Computational Geosciences (2023) 27:649–662
https://doi.org/10.1007/s10596-023-10224-3

ORIGINAL PAPER

Solving the fixed gravimetric boundary value problem by the finite element method using mapped infinite elements.

Marek Macák[1] · Zuzana Minarechová[1] · Lukáš Tomek[1] · Róbert Čunderlík[1] · Karol Mikula[1,2]

Received: 28 July 2022 / Accepted: 25 May 2023 / Published online: 5 July 2023

Abstract
The numerical approach for solving the fixed gravimetric boundary value problem (FGBVP) based on the finite element method (FEM) with mapped infinite elements is developed and implemented. In this approach, the 3D semi-infinite domain outside the Earth is bounded by the triangular discretization of the whole Earth's surface and extends to infinity. Then the FGBVP consists of the Laplace equation for unknown disturbing potential which holds in the domain, the oblique derivative boundary condition (BC) given directly at computational nodes on the Earth's surface, and regularity of the disturbing potential at infinity. In this way, it differs from previous FEM approaches, since the numerical solution is not fixed by the Dirichlet BC on some part of the boundary of the computational domain. As a numerical method, the FEM with finite and mapped infinite triangular prisms has been derived and implemented. In experiments, at first, a convergence of the proposed numerical scheme to the exact solution is tested. Afterwards, a numerical study is focused on a reconstruction of the harmonic function (EGM2008) above the Earth's topography. Here, a special discretization of the Earth's surface which is able to fulfil the conditions that arise from correct geometrical properties of finite elements, and it is suitable for parallel computing is implemented. The obtained solutions at nodes on the Earth's surface as well as nodes that lie approximately at the altitude of the GOCE satellite mission have been tested.

Keywords Fixed gravimetric boundary value problem · Oblique derivative boundary condition · 3D semi-infinite domain · Finite element method · Mapped infinite element · Global gravity field modelling · Reconstruction of the EGM2008

1 Introduction

In mathematical modelling, there are some problems which are obviously unbounded like the object of our study - gravity of the Earth. However, also many other engineering problems, where, e.g., one concentrates only on a small subdomain of an extremely large domain may be also termed as infinite domain problems, since in these cases, the total area or volume can be for practical purposes taken as infinite. These mathematical models then occur in various engineering applications, e.g. in elasticity [21, 29], potential problems [10], fluid flow [17, 39, 42], etc. In the finite element analysis these problems are solved in various ways, all of which have advantages and disadvantages. The simplest way is to truncate the domain by adding some artificial boundary with the prescribed artificial BC at some large but finite distance, see e.g. [12, 14]. In our approach, we will use the so-called mapped infinite elements (MIE), which were originally pioneered by Bettess in [2]. We will show that such an approach provides an efficient and effective alternative to other well-known numerical approaches.

Gravity field modelling is usually performed as solving the so-called geodetic boundary value problems (BVPs). In our study, we will focus on one of them, namely the fixed gravimetric boundary value problem (FGBVP) that repre-

✉ Zuzana Minarechová
zuzana.minarechova@stuba.sk

Marek Macák
marek.macak@stuba.sk

Lukáš Tomek
lukas.tomek@stuba.sk

Róbert Čunderlík
robert.cunderlik@stuba.sk

Karol Mikula
karol.mikula@stuba.sk

[1] Faculty of Civil Engineering, Slovak University of Technology, Radlinského 11, Bratislava 810 05, Slovakia

[2] Algoritmy:SK s.r.o., Šulekova , Bratislava 81106, Slovakia

sents an exterior oblique derivative BVP for the Laplace equation, cf. Koch and Pope [20], Freeden and Kersten [15], Bjerhammar and Svensson [4], Holota [16]. As the oblique derivative boundary conditions (BC) given on the discretized Earth's surface will be taken surface gravity disturbances. The detailed overview of various procedures for solving the oblique derivative BVP can be found, e.g., in Minarechová et al. [34].

With an expansion of high-performance computing (HPC) facilities in the last decades, approaches based on numerical methods have become a powerful and efficient tool finding applications also in gravity field modelling. The pioneering studies on numerical methods applied to gravity field modelling were based on the finite element method (FEM), cf. Meissl [32] or Shaofeng and Dingbo [38]. Later, the finite difference method (FDM) was applied by Keller [18], and the indirect boundary element method (BEM) approach was developed by Klees [19] and Lehmann and Klees [22]. Afterwards, the direct BEM approach was introduced by Čunderlík et al. [7] and Čunderlík and Mikula [8]. The oblique derivative BVP treated by BEM was discussed in Čunderlík et al. [9]. At that time, also new studies on FEM were published, cf. Fašková et al. [12, 14] and Mráz et al. [35]. The FEM with MIE for BVP with Neumann BC has been introduced by Šprlák et al. [41]. The first application of the finite volume method (FVM) to gravity field modelling was introduced by Fašková [13] and its parallel implementation by Minarechová et al. [33]. The FVM applied to the oblique derivative BVP has been studied in Macák et al. [24, 26, 27]. Lately, Medľa et al. [31] presented the FVM for solving the oblique derivative BVP on 3D unstructured meshes above the real Earth's topography and Droniou et al. [11] analysis of FVM for elliptic equations with oblique derivatives. Recently, Yin and Sneeuw in [43] published a new approach to the gravitational field modelling by using CFD (Computational fluid dynamics) techniques based on FEM, and Macák et al. in [28] and Minarechová et al. in [34] applied the FEM for local solutions of the oblique derivative BVP.

In previous numerical approaches based on FEM or FVM, see for example [12–14, 24, 26–28, 31, 33, 34, 41], a condition of the regularity at infinity has been abandoned by introducing an artificial upper boundary approximately at altitudes of the GOCE satellite orbits. Here the FEM or FVM numerical solutions have been fixed by the prescribed Dirichlet BC in terms of the disturbing potential. In this paper we avoid this drawback and the presented FEM approach is developed to solve the original FGBVP including the condition of the regularity at infinity. This is a main contribution of this study in comparison with the previous ones.

The paper is organized as follows. In Section 2, we formulate the FGBVP with the oblique derivative BC. In Section 3, we derive a numerical scheme of the FEM with MIE for the FGBVP. Then numerical experiments are presented in Section 4 that aim to test accuracy of the developed approach. Here we also describe a special triangular discretization of the Earth's surface that is suitable for FEM. The paper ends with Conclusion and summary.

2 Formulation of the FGBVP with the oblique derivative BC

Let us consider the FGBVP, cf. [4, 16, 20]:

$$\Delta T(\mathbf{x}) = 0, \quad \mathbf{x} \in \Omega, \tag{1}$$

$$\nabla T(\mathbf{x}) \cdot \mathbf{s}(\mathbf{x}) = -\delta g(\mathbf{x}), \quad \mathbf{x} \in \Gamma, \tag{2}$$

$$T(\mathbf{x}) \to 0, \quad \text{as} \quad |\mathbf{x}| \to \infty, \tag{3}$$

where the computational domain Ω, see Fig. 1, is bounded by the boundary Γ, i.e., the Earth's surface, from the bottom and extends to infinity. $T(\mathbf{x})$ stands for the disturbing potential defined as a difference between the real and normal gravity potential at any point $\mathbf{x} = (x, y, z)$, $\delta g(\mathbf{x})$ is the gravity disturbance, and the vector $\mathbf{s}(\mathbf{x}) = -\nabla U(\mathbf{x})/|\nabla U(\mathbf{x})|$ is the unit vector normal to the equipotential surface of the normal potential $U(\mathbf{x})$ at any point $\mathbf{x}$.

3 Solution to the FGBVP with the oblique derivative BC by the FEM with MIE

In our approach, we follow the fundamental principles of FEM presented by Reddy in [37] with the theory of MIE

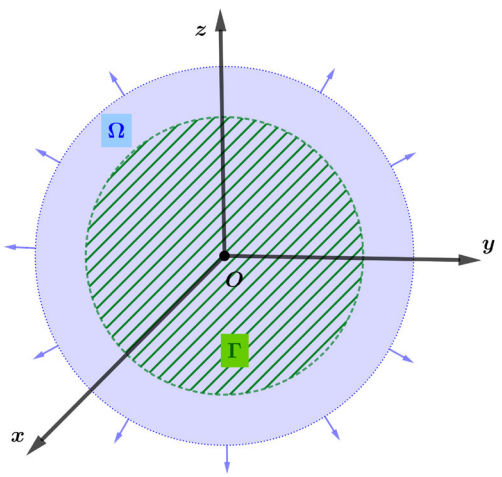

Fig. 1 The semi-infinite computational domain Ω for global gravity field modelling. It is bounded from the bottom by the boundary Γ discretizing the Earth's surface, and extends to infinity in the vertical direction

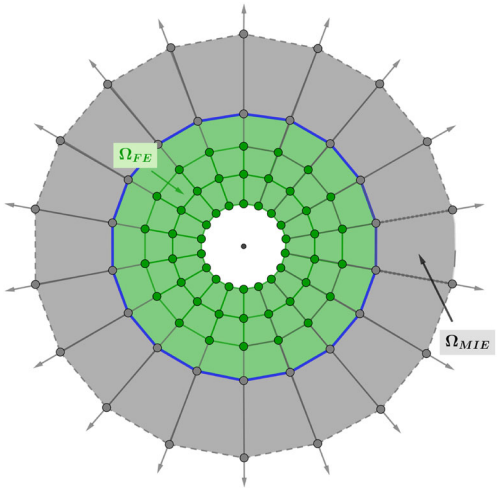

Fig. 2 Brief sketch of the computational domain Ω meshed with finite elements depicted by green, and one layer of mapped infinite elements depicted by grey

published by Bettes in [2, 3], Marques and Owen in [29] or Zienkiewicz et al. in[44, 45].

3.1 Discretization of the computational domain

The FEM is a numerical method that assumes discretization of the whole computational domain Ω by a union of elements Ω^e, $e = 1, ..., \mathcal{N}$, where $\mathcal{N}$ denotes the number of elements in the domain Ω. In our FEM approach, we divide the semi-infinite computational domain Ω into two parts, see Fig. 2, where the lower one, denoted by Ω_{FE}, is meshed with finite elements and the upper one, Ω_{MIE}, is meshed with one layer of infinite elements.

For our purpose - to fit irregular boundary Γ, we have chosen triangular prisms, i.e., finite pentahedral elements with six nodes and five faces, and corresponding mapped infinite pentahedral elements with nine nodes and five faces, see Fig. 3. In this way, we divide the computational domain Ω into n_1, n_2, n_3 elements in the latitudinal, longitudinal and vertical direction, respectively, and to specify the position of an element Ω^e we use indexes k, l, m, where $k = 1, ..., n_1$, $l = 1, ..., n_2$ and $m = 1, ..., n_3$.

3.2 Derivation of the weak formulation on the element

Let us consider an arbitrary element Ω^e from our finite element discretization with indexes $k = 1, ..., n_1$, $l = 1, ..., n_2$ and $m = 2, ..., n_3$. We multiply the differential equation (1) by a weight function w and using Green's identity (we omit $(\mathbf{x})$ to simplify the notation in the following equations) we obtain the weak formulation (WF) of (1) over an arbitrary above defined element Ω^e

$$\int_{\Omega^e} \nabla T \cdot \nabla w \, \mathrm{d}x\mathrm{d}y\mathrm{d}z = \int_{\partial\Omega^e} \nabla T \cdot \mathbf{n} \, w \, \mathrm{d}\sigma, \tag{4}$$

where $\mathbf{n}$ denotes the unit normal to $\partial\Omega^e$.

Since on the bottom boundary Γ the oblique derivative BC (2) is prescribed, for the row of elements that lie on this boundary (see Fig. 4, elements depicted by yellow), i.e., $k = 1, ..., n_1, l = 1, ..., n_2$ and $m = 1$, we modify (4) in such a way that has been also presented, for instance, in [28] or [34]. We split the oblique vector $\mathbf{s}$ into one normal and two tangential components

$$\mathbf{s} = c_1\mathbf{n} + c_2\mathbf{t}_1 + c_3\mathbf{t}_2, \tag{5}$$

where $\mathbf{n}$ is the normal vector and $\mathbf{t}_1, \mathbf{t}_2$ are tangent vectors to $\Gamma^e \subset \partial\Omega^e \subset R^3$, where Γ^e denotes the bottom boundary of an element Ω^e.

Then we replace vector $\mathbf{s}$ in (2) by (5) to obtain

$$\nabla T \cdot \mathbf{s} = c_1 \nabla T \cdot \mathbf{n} + c_2 \nabla T \cdot \mathbf{t}_1 + c_3 \nabla T \cdot \mathbf{t}_2 = -\delta g. \tag{6}$$

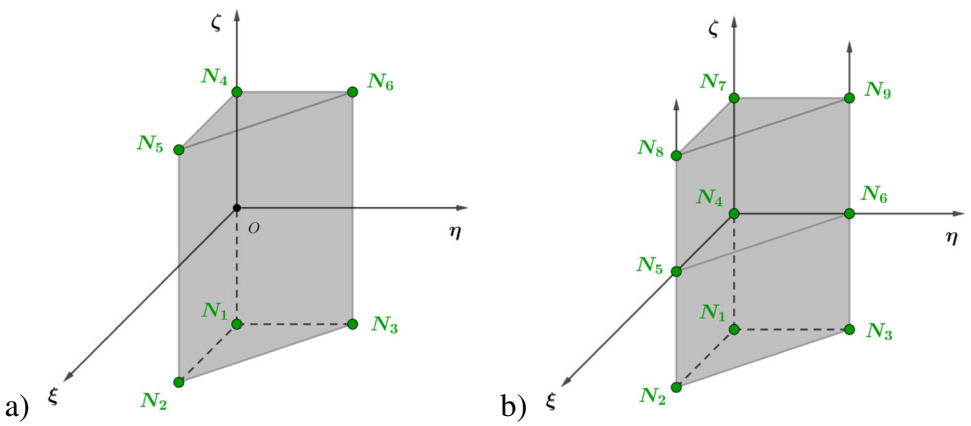

Fig. 3 Types of elements used in our computations: a) the finite pentahedral elements with six nodes, and b) the mapped infinite pentahedral elements with nine nodes. Isoparametric coordinates are within intervals $0 \le \xi \le 1, 0 \le \eta \le 1$ and $-1 \le \zeta \le 1$

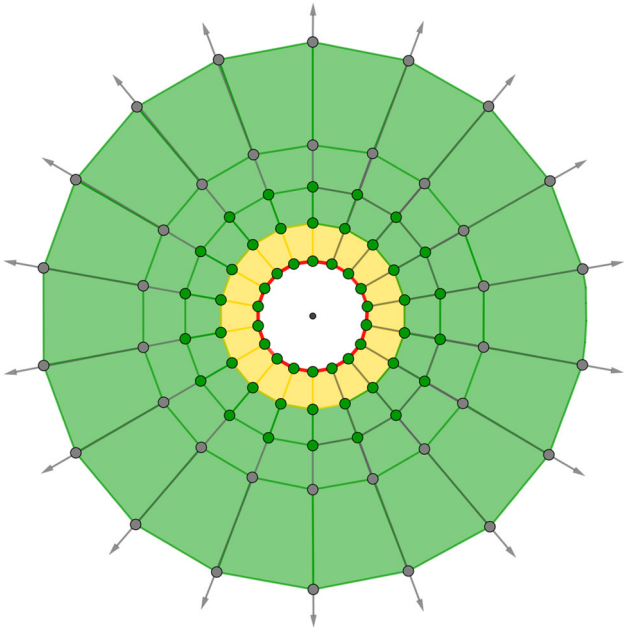

Fig. 4 Brief sketch of the computational domain Ω for derivation of the WF. Due to the oblique derivative BC prescribed on Γ (depicted by red), for the row of elements depicted by yellow we have to derive a different WF in comparison to the rest of the elements depicted by green

From (6) we express the normal derivative

$$\nabla T \cdot \mathbf{n} = \frac{-\delta g}{c_1} - \frac{c_2}{c_1}\frac{\partial T}{\partial \mathbf{t}_1} - \frac{c_3}{c_1}\frac{\partial T}{\partial \mathbf{t}_2}, \tag{7}$$

where we assume that $c_1 \neq 0$, since in practical experiments we always use a 'nonzero' horizontal resolution of the grid points that discretized the real Earth's surface. In such manner, $\mathbf{s}$ is never perpendicular to $\mathbf{n}$, so the assumption $c_1 \neq 0$ is always fulfilled.

Now, we insert (7) to (4) to get

$$\begin{aligned} &\int_{\Omega^e} \nabla T \cdot \nabla w \,\mathrm{d}x\mathrm{d}y\mathrm{d}z = \\ &= \int_{\Gamma^e} \left(\frac{-\delta g}{c_1} - \frac{c_2}{c_1}\frac{\partial T}{\partial \mathbf{t}_1} - \frac{c_3}{c_1}\frac{\partial T}{\partial \mathbf{t}_2} \right) w \,\mathrm{d}\sigma + \int_{\partial\Omega^e \setminus \Gamma^e} \nabla T \cdot \mathbf{n}\, w \,\mathrm{d}\sigma. \end{aligned} \tag{8}$$

After some rearrangement, we have

$$\begin{aligned} &\int_{\Omega^e} \nabla T \cdot \nabla w \,\mathrm{d}x\mathrm{d}y\mathrm{d}z + \frac{c_2}{c_1}\int_{\Gamma^e} \frac{\partial T}{\partial \mathbf{t}_1}\, w \,\mathrm{d}\sigma + \frac{c_3}{c_1}\int_{\Gamma^e} \frac{\partial T}{\partial \mathbf{t}_2}\, w \,\mathrm{d}\sigma = \\ &= \int_{\Gamma^e} \frac{-\delta g}{c_1}\, w \,\mathrm{d}\sigma + \int_{\partial\Omega^e \setminus \Gamma^e} \nabla T \cdot \mathbf{n}\, w \,\mathrm{d}\sigma. \end{aligned} \tag{9}$$

Thus we have obtained the weak formulation (4) or (9) of the BVP (1) - (3) on every element Ω^e of our finite element discretization. The study of weak solution of the oblique derivative BVP is included in the book by Lieberman [23].

3.3 Solution by the Finite Element Method

For a finite pentahedral element Ω^e with six nodes, see Fig. 3 a), we can write

$$T \approx T^e = \sum_{j=1}^{6} T_j^e \psi_j(x, y, z), \tag{10}$$

i. e., we take an approximation of the unknown value T as T^e, a linear combination of basis functions ψ_j with coefficients T_j^e, $j = 1, ..., 6$. Then we substitute it into the weak formulation (4), namely for elements Ω^e with indexes $k = 1, ..., n_1$, $l = 1, ..., n_2$ and $m = 2, ..., n_3 - 1$ (see Fig. 5, elements depicted by green), and consider ψ_i for weight function w. We obtain the i^{th} equation in the form

$$\begin{aligned} &\sum_{j=1}^{6} T_j^e \int_{\Omega^e} \frac{\partial \psi_j}{\partial x}\frac{\partial \psi_i}{\partial x} + \frac{\partial \psi_j}{\partial y}\frac{\partial \psi_i}{\partial y} + \frac{\partial \psi_j}{\partial z}\frac{\partial \psi_i}{\partial z} \,\mathrm{d}x\mathrm{d}y\mathrm{d}z = \\ &= \sum_{j=1}^{6} \int_{\partial\Omega^e} q_n\, \psi_i \,\mathrm{d}x\mathrm{d}y, \end{aligned} \tag{11}$$

where $q_n = \nabla T \cdot \mathbf{n}$ denotes the projection of the vector ∇T along the unit normal $\mathbf{n}$.

For the row of elements Ω^e given by indexes $k = 1, ..., n_1$, $l = 1, ..., n_2$ and $m = 1$ (see Fig. 5, elements

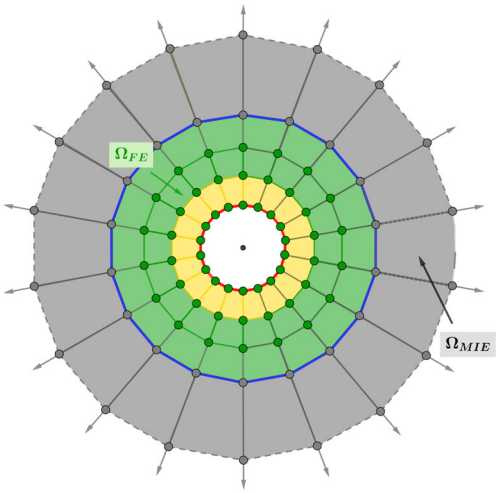

Fig. 5 Brief sketch for a derivation of the i^{th} equation on every element. The i^{th} equation depends on the vertical position of the element Ω^e

depicted by yellow), we follow the same way and after inserting (10) into (9) and considering $w = \psi_i$, we obtain the i^{th} equation in the form

$$\sum_{j=1}^{6} T_j^e \left(\int_{\Omega^e} \frac{\partial \psi_j}{\partial x}\frac{\partial \psi_i}{\partial x} + \frac{\partial \psi_j}{\partial y}\frac{\partial \psi_i}{\partial y} + \frac{\partial \psi_j}{\partial z}\frac{\partial \psi_i}{\partial z}\,\mathrm{d}x\mathrm{d}y\mathrm{d}z \right) + \\ + \sum_{j=1}^{3} T_j^e \left(\frac{c_2}{c_1}\int_{\Gamma^e} \frac{\partial \psi_j}{\partial \mathbf{t}_1}\psi_i\,\mathrm{d}x\mathrm{d}y + \frac{c_3}{c_1}\int_{\Gamma^e} \frac{\partial \psi_j}{\partial \mathbf{t}_2}\psi_i\,\mathrm{d}x\mathrm{d}y \right) = \\ = \sum_{j=1}^{3}\int_{\Gamma^e} \frac{-\delta g_j}{c_1}\psi_i\,\mathrm{d}x\mathrm{d}y + \sum_{j=1}^{6}\int_{\partial\Omega^e\setminus\Gamma^e} q_n\,\psi_i\,\mathrm{d}x\mathrm{d}y, \tag{12}$$

where index $j = 1, \ldots, 3$ refers to nodes of the element Ω^e that lie on the bottom boundary Γ of the computational domain Ω. As we can see in Eq. (12), there are 2 tangent vectors corresponding to the nodes lying on the bottom boundary of the element belonging to Γ.

Finally, for the mapped infinite pentahedral element Ω^e with nine nodes, see Fig. 3 b), we can write

$$T \approx T^e = \sum_{j=1}^{9} T_j^e \psi_j(x, y, z). \tag{13}$$

We substitute (13) for elements Ω^e with indexes $k = 1, \ldots, n_1$, $l = 1, \ldots, n_2$ and $m = n_3$ (see Fig. 5, elements depicted by grey) into (4), consider ψ_i for weight function w and we obtain the i^{th} equation in the form

$$\sum_{j=1}^{9} T_j^e \int_{\Omega^e} \frac{\partial \psi_j}{\partial x}\frac{\partial \psi_i}{\partial x} + \frac{\partial \psi_j}{\partial y}\frac{\partial \psi_i}{\partial y} + \frac{\partial \psi_j}{\partial z}\frac{\partial \psi_i}{\partial z}\,\mathrm{d}x\mathrm{d}y\mathrm{d}z = \\ = \sum_{j=1}^{9}\int_{\partial\Omega^e} q_n\,\psi_i\,\mathrm{d}x\mathrm{d}y, \tag{14}$$

where $q_n = \nabla T \cdot \mathbf{n}$ again denotes the projection of the vector ∇T along the unit normal $\mathbf{n}$.

3.3.1 Shape and mapped functions

The basis function ψ_i is the piecewise quadratic function and it is uniquely determined by choosing value 1 at N_i and 0 at every N_j, $i \neq j$, cf. [5]. In our approach, we will work with isoparametric coordinates ξ, η, ζ in local coordinate system, so we rewrite (10) and (13) in the form

$$T \approx T^e = \sum_{j=1}^{6} T_j^e \psi_j(x, y, z) = \sum_{j=1}^{6} T_j^e \psi_j(\xi, \eta, \zeta), \tag{15}$$

$$T \approx T^e = \sum_{j=1}^{9} T_j^e \psi_j(x, y, z) = \sum_{j=1}^{9} T_j^e \psi_j(\xi, \eta, \zeta), \tag{16}$$

Table 1 The shape functions $\psi_i(\xi, \eta, \zeta)$ for the finite pentahedral element with six nodes N_i defined by isoparametric coordinates ξ, η and ζ

N_i	ξ	η	ζ	Shape functions $\psi_i(\xi, \eta, \zeta)$
N_1	0	0	-1	$(1-\xi-\eta)(1-\zeta)/2$
N_2	1	0	-1	$\xi(1-\zeta)/2$
N_3	0	1	-1	$\eta(1-\zeta)/2$
N_4	0	0	1	$(1-\xi-\eta)(1+\zeta)/2$
N_5	1	0	1	$\xi(1+\zeta)/2$
N_6	0	1	1	$\eta(1+\zeta)/2$

where the transformation between local coordinates ξ, η, ζ and global coordinates x, y, z is given by

$$\begin{bmatrix} \frac{\partial \psi_i}{\partial \xi} \\ \frac{\partial \psi_i}{\partial \eta} \\ \frac{\partial \psi_i}{\partial \zeta} \end{bmatrix} = \begin{bmatrix} \frac{\partial x}{\partial \xi} & \frac{\partial y}{\partial \xi} & \frac{\partial z}{\partial \xi} \\ \frac{\partial x}{\partial \eta} & \frac{\partial y}{\partial \eta} & \frac{\partial z}{\partial \eta} \\ \frac{\partial x}{\partial \zeta} & \frac{\partial y}{\partial \zeta} & \frac{\partial z}{\partial \zeta} \end{bmatrix} \begin{bmatrix} \frac{\partial \psi_i}{\partial x} \\ \frac{\partial \psi_i}{\partial y} \\ \frac{\partial \psi_i}{\partial z} \end{bmatrix}. \tag{17}$$

Then the shape functions $\psi_i(\xi, \eta, \zeta)$ for finite pentahedral element with six nodes (see Fig.3 a)) in local coordinate system that is used to mesh Ω_{FE} are defined in Table 1.

Since in FGBVP (1) - (3), the computational domain Ω tends to infinity only in the vertical direction, we start by explaining MIE on one-dimensional problem and then we will apply this idea on our FGBVP.

Let us have the one-dimensional element Ω^e which extends from node N_1 with coordinate x_1 through N_2 with coordinate x_2 to the point N_3 infinity, see Fig 6. Then let us have the so-called Pole that is the point O with coordinate x_0 and lies on the line that passes through points N_1, N_2 and N_3. The relationship between coordinates x_0, x_1 and x_2 is given by

$$x_2 = 2x_1 - x_0. \tag{18}$$

It is obvious that the position of the Pole has an impact on the results and has to be chosen very carefully, since an incorrect Pole position can lead to a distortion of the map-

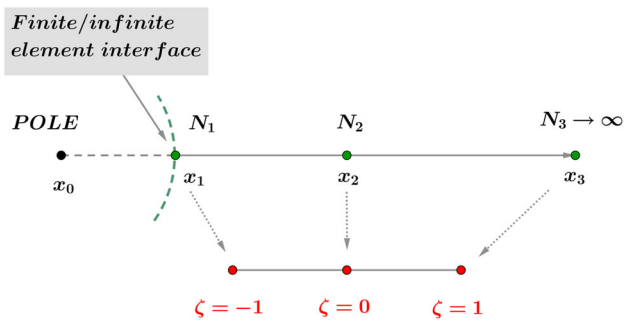

Fig. 6 Brief sketch of one-dimensional MIE Ω^e

ping, cf. [2, 3, 44, 45]. However, due to geometry of our computational domain Ω, see Fig. 1, it is natural to have $O = [0, 0, 0]$, so we will not discuss the problem of incorrect Pole position in detail. Then this element is mapped onto the parent element defined in the local coordinate system in the range $-1 < \zeta < 1$ using formula

$$x(\zeta) = M_1(\zeta)x_1 + M_2(\zeta)x_2, \tag{19}$$

where

$$M_1(\zeta) = \frac{-2\zeta}{1-\zeta}, \tag{20}$$

$$M_2(\zeta) = \frac{1+\zeta}{1-\zeta}. \tag{21}$$

It is obvious from (19)-(21) that $\zeta = -1, 0, 1$ correspond to the global positions of x_1, x_2, ∞, respectively. Then for infinite pentahedral element with nine nodes N_i, we obtain the mapping functions $M_i(\xi, \eta, \zeta)$ by multiplying (21) with the shape functions $\psi_i(\xi, \eta, \zeta)$ where directions ξ and η are finite. These mapping functions $M_i(\xi, \eta, \zeta)$ can be seen in Table 2.

We remain that for more details about MIE, see e.g. [2, 3] or [44, 45].

Now we can write (11) and (12) in a compact matrix form

$$\mathbf{K}^e\,\mathbf{T}^e = \mathbf{Q}^e, \tag{22}$$

where $\mathbf{K}^e = [K_{ij}]$ stands for an element stiffness matrix, $\mathbf{T}^e = (T_1, ..., T_6)$ is a column vector of unknowns and $\mathbf{Q}^e$ denotes the right-hand side vector.

To evaluate element matrices and vectors we proceed the following way. We choose one basis function ψ_i per vertex N_i^e and we differentiate the basis functions with respect to a position of each node. To calculate two integrals over a boundary Γ in Eq. (11) which include a tangential derivative,

Table 2 The mapping functions $M_i(\xi, \eta, \zeta)$ for the infinite pentahedral element with nine nodes N_i which extends to infinity in the vertical direction. Values ξ, η and ζ denote isoparametric coordinates of nodes

N_i	ξ	η	ζ	Mapping functions $M_i(\xi, \eta, \zeta)$
N_1	0	0	-1	$(1-\xi-\eta)\,(-2\zeta)/(1-\zeta)$
N_2	1	0	-1	$\xi(-2\zeta)/(1-\zeta)$
N_3	0	1	-1	$\eta(-2\zeta)/(1-\zeta)$
N_4	0	0	0	$(1-\xi-\eta)\,(1+\zeta)/(1-\zeta)$
N_5	1	0	0	$\xi(1+\zeta)/(1-\zeta)$
N_6	0	1	0	$\eta(1+\zeta)/(1-\zeta)$
N_7	0	0	1	-
N_8	1	0	1	-
N_9	0	1	1	-

we approximate derivatives in tangential direction like in the FDM, i.e., using values of basis functions at nodes N_i of element e we have

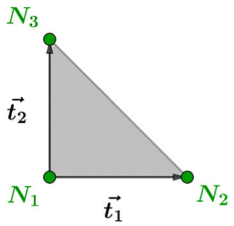

$$\frac{\partial \psi_j^{(e)}}{\partial \mathbf{t}_1} \approx \frac{\psi_j^{(e)}(N_2) - \psi_j^{(e)}(N_1)}{d(N_1, N_2)}, \tag{23}$$

$$\frac{\partial \psi_j^{(e)}}{\partial \mathbf{t}_2} \approx \frac{\psi_j^{(e)}(N_3) - \psi_j^{(e)}(N_1)}{d(N_1, N_3)}, \tag{24}$$

where d denotes the distance between two neighbouring nodes. The similar idea of approximating derivatives in tangential direction like in the FDM, however for hexahedral elements, has been presented in [34].

3.4 Assembly of element equations

Finally, we assemble all element equations using two principles, see Reddy [37]:

(i) continuity of primary variables at the interelement nodes. It means that nodal values T_j^e and T_j^{e+1} of two adjacent elements Ω^e and Ω^{e+1} at the connecting nodes have to be the same.
(ii) balance of secondary variables in a weighted-integral sense, see Reddy [37].

In this manner, we obtain the global linear system of equations with a column vector of unknown global nodal values $\mathbf{T}$

$$\mathbf{KT} = \mathbf{Q}, \tag{25}$$

where the matrix $\mathbf{K}$ is sparse, since most of its entries are zero, and positive definite, and $\mathbf{Q}$ is the column vector whose entries are also almost zero except that for nodes with the prescribed oblique derivative BC (2).

4 Numerical experiments

To test the proposed numerical scheme, we present several numerical experiments. In them, results of the proposed method are compared to either exact, in testing experiments, or EGM2008, in experiments with gravity data, solutions.

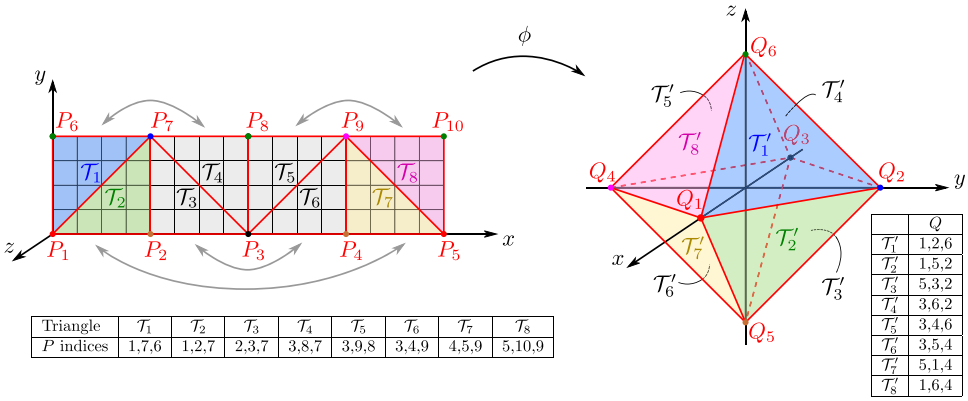

Triangle	$\mathcal{T}_1$	$\mathcal{T}_2$	$\mathcal{T}_3$	$\mathcal{T}_4$	$\mathcal{T}_5$	$\mathcal{T}_6$	$\mathcal{T}_7$	$\mathcal{T}_8$
P indices	1,7,6	1,2,7	2,3,7	3,8,7	3,9,8	3,4,9	4,5,9	5,10,9

	Q
$\mathcal{T}'_1$	1,2,6
$\mathcal{T}'_2$	1,5,2
$\mathcal{T}'_3$	5,3,2
$\mathcal{T}'_4$	3,6,2
$\mathcal{T}'_5$	3,4,6
$\mathcal{T}'_6$	3,5,4
$\mathcal{T}'_7$	5,1,4
$\mathcal{T}'_8$	1,6,4

Fig. 7 Piecewise affine mapping of rectangle (meshed with $n = 4$) onto regular octahedron

In testing experiments, the numerical scheme is qualified according to the value of the experimental order of convergence (EOC), see e.g. [28], that can be determined by comparing numerical solutions and exact solutions on subsequently refined grids. In experiments with the reconstruction of EGM2008 data, the obtained numerical solution is compared with the disturbing potential generated from EGM2008 directly and is qualified according to the statistics of residuals. To solve the nonsymmetric linear system, BiCGSTAB(l) linear solver with $l = 8$, cf. [40], has been implemented. To save the memory, only nonzero coefficients were stored. These large-scale parallel computations were performed on 4 nodes of our cluster with 1.0 TB of distributed memory (each node consists of four 8-core CPUs with 256 GB RAM). Thanks to the NUMA (Non-Uniform Memory Access) architecture of each node, we have implemented an MPI and OpenMP parallelization, see [25].

4.1 Discretization of the bottom boundary

As we have mentioned in the beginning, the FEM requires elements to meet some geometrical specifications, as well as detailed global gravity modelling requires parallel computing. In this section, we describe the generation of the bottom boundary mesh, which is suitable for the presented numerical approach. The final triangle mesh is geometrically a standard octahedron sphere, usually created by subdividing the faces of an octahedron. However, we use a numbering of vertices and faces, which is suitable for a parallelisation. The mesh generation is based on mapping of a rectangle to regular octahedron, see Fig. 7. The process of mesh generation is then performed in several steps described below.

1. *Planar square mesh.* At first, we create a regular 4 n-square mesh of the rectangle $[0, 4] \times [0, 1]$, see Fig. 7 a). In this way, we have obtained the mesh that consists of $4n^2$ squares and $(4n+1)(n+1)$ nodes $N_j = (N_{j,1}, N_{j,2}, 0)^T$, where $N_{j,1}$, $N_{j,2}$ denote x and y coordinate, respectively. Then this rectangle is divided into 8 auxiliary triangles $\mathcal{T}_1, \ldots, \mathcal{T}_8$, see Fig. 7 a).
2. *Mapping to octahedron.* Then we map the rectangle onto the regular octahedron by a piecewise affine mapping $\phi : \mathbb{R}^3 \to \mathbb{R}^3$. It means that each triangle $\mathcal{T}_i$ with corresponding nodes N_j is mapped onto the face $\mathcal{T}'_i$ of the octahedron, see Fig. 7, by the affine mapping $\phi_i : \mathbb{R}^3 \to \mathbb{R}^3$ defined as

$$\phi_i(X) = M_i(X - G_i) + G'_i, \qquad \text{for } X \in \mathcal{T}_i, \tag{26}$$

where G_i, G'_i denote the centroids of the triangles $\mathcal{T}_i$, $\mathcal{T}'_i$, respectively, and M_i is a 3×3 matrix. Therefore, the mapping ϕ is defined as $\phi(X) := \phi_i(X)$ for $X \in \mathcal{T}_i$. The nodes N_j on rectangle are mapped to the nodes $N'_j := \phi(N_j)$ on the octahedron.

The construction of the matrix M_i is done as follows. Let $X_1X_2X_3$ denote a domain triangle with centroid G_i and $X'_1X'_2X'_3$ a range triangle with centroid G'_i. Then $\bar{X}_k := X_k - G_i$ and $\bar{X}'_k := X'_k - G'_i$ denote the coordinates of

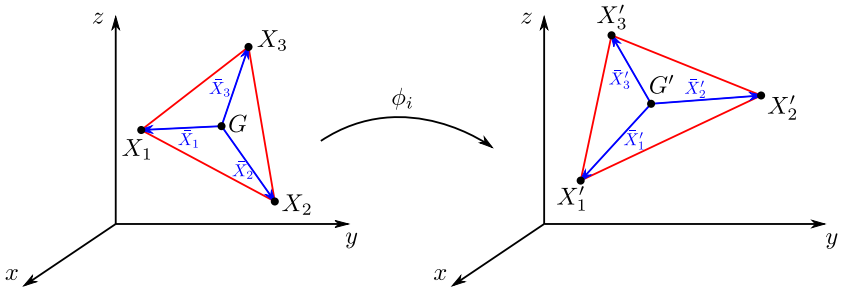

Fig. 8 Affine transformation ϕ_i of a triangle X_1X_2, X_3

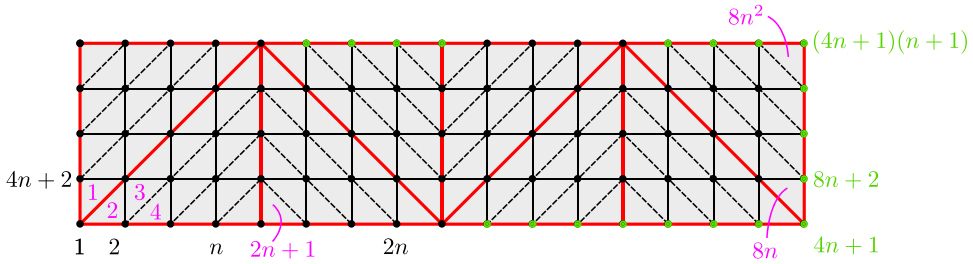

Fig. 9 Final splitting and numbering of nodes and mesh triangles is depicted on rectangle. Duplicate nodes are highlighted by green

vertices w.r.t. centroid, see Fig. 8. If we plug the vertices X_k and $X'_k = \phi_i(X_k)$ into the equation (26), we obtain a linear system $M_i \bar{X}_k = \bar{X}'_k$, $k = 1, 2, 3$ with 9 equations and 9 unknown elements of the matrix M_i. Unfortunately, the equations are not linearly independent, because $\bar{X}_1 + \bar{X}_2 + \bar{X}_3 = 0$ and $\bar{X}'_1 + \bar{X}'_2 + \bar{X}'_3 = 0$. To obtain an independent system of equations, we can include, e.g., normal vectors $\bar{X}_1 \times \bar{X}_2$, $\bar{X}'_1 \times \bar{X}'_2$ instead of $\bar{X}_3$, $\bar{X}'_3$, respectively. Therefore, we have to solve the system

$$\begin{aligned} M_i \bar{X}_1 &= \bar{X}'_1, \\ M_i \bar{X}_2 &= \bar{X}'_2, \\ M_i (\bar{X}_1 \times \bar{X}_2) &= (\bar{X}'_1 \times \bar{X}'_2). \end{aligned}$$

If we define 3×3 matrices

$$\bar{X} := \left[\bar{X}_1, \bar{X}_2, \bar{X}_1 \times \bar{X}_2\right] \quad \text{and} \quad \bar{X}' := \left[\bar{X}'_1, \bar{X}'_2, \bar{X}'_1 \times \bar{X}'_2\right],$$

we see that the matrix M_i is given by $M_i = \bar{X}' \bar{X}^{-1}$.

3. *Gluing.* The mapping ϕ glues the triangle edges on the boundary of the rectangle. There are 5 gluings together of pairs of triangle edges, 4 of them are indicated by grey arrows in Fig. 7, left. The last one glues the left and right side of the rectangle. As a result, corresponding nodes N'_j need to be identified, see Fig. 9.
4. *Normalisation to unit sphere.* The nodes N'_j on the octahedron are mapped to the unit sphere simply by normalisation $\hat{N}_j := N'_j / \|N'_j\|$.
5. *Scaling to the WGS84 ellipsoid.* Finally, we scale the unit sphere to the ellipsoid to obtain final nodes $V_j := \mathrm{diag}(a, a, b)\hat{N}_j$, where diag stands for diagonal matrix, and a is the semi-major axis and b is the polar semi-minor axis of the WGS84 ellipsoid.
6. *Splitting quads.* In the last step, we split each quad diagonally to create two triangles. The direction of splitting as well as numbering of the triangles and nodes is shown in Fig. 9.

In numerical computations we use meshes with $n = 2^l$, where l is the level of refinement of the mesh. Examples of two coarse meshes (level $l = 2, 4$) are visualised in Fig. 10. Mesh statistics for levels $l = 1, \ldots, 10$ is presented in Table 3.

4.2 Testing numerical experiments

As usual in numerical mathematics, at first we test the stability and behaviour of the numerical scheme derived in Section 3 by investigating its EOC. In these testing numerical experiments we have chosen the well-known example, gravitational potential generated by a homogeneous sphere,

Table 3 *Mesh statistics for meshes with the refinement level l.* The number of divisions of rectangle in y direction is calculated as $n = 2^l$, the number of quads as $4n^2$, the number of triangles as $8n^2$, the number of vertices (nodes) on the rectangle as $(4n+1)(n+1)$ and the number of duplicate vertices on ellipsoid as $5n - 1$

l	n	No. of quads	No. of triangles	No. of nodes	No. of dupl. nodes
1	2	16	32	27	9
2	4	64	128	85	19
3	8	256	512	297	39
4	16	1024	2048	1105	79
5	32	4096	8192	4257	159
6	64	16384	32768	16705	319
7	128	65536	131072	66177	639
8	256	262144	524288	263425	1279
9	512	1048576	2097152	1051137	2559
10	1024	4194304	8388608	4199425	5119

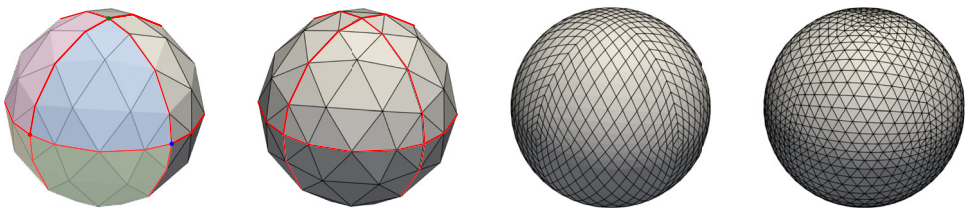

Fig. 10 Quad and triangular meshes for levels $l = 2$ and $l = 4$

Table 4 *Testing experiment 1*: Statistics of residuals $[m^2 s^{-2}]$ between the obtained nodal numerical solution and the exact solution at the bottom boundary Γ, where Min, Max, Mean denote the minimum, maximum and mean value of residuals, respectively. STD stands for the standard deviation calculated as $\sqrt{1/N \sum_{i=1}^{N} (\text{residuals}_i)^2}$, where N is the number of nodes

No. of nodes	Min	Max	Mean	Median	STD	EOC
64x16x4	-0.5678	0.2036	-0.1057	-0.1239	0.1690	-
128x32x8	-0.1705	0.0460	-0.0282	-0.0317	0.0434	1.9597
256x64x16	-0.0490	0.0109	-0.0072	-0.0078	0.0112	1.9533
512x128x32	-0.0138	0.0027	-0.0018	-0.0019	0.0028	2.0134
1024x256x64	-0.0038	0.0007	-0.0005	-0.0005	0.0007	2.0076

Table 5 *Testing experiment 2*: Statistics of residuals $[m^2 s^{-2}]$ between the obtained numerical solution and the exact solution on the bottom boundary Γ

$H_{\Omega_{FE}}$	No. of nodes	Min	Max	Mean	Median	STD
500 $[km]$	256x64x16	-0.0490	0.0109	-0.0072	-0.0078	0.0112
1000 $[km]$	256x64x32	-0.0487	0.0109	-0.0072	-0.0078	0.0111
2000 $[km]$	256x64x64	-0.0486	0.0108	-0.0072	-0.0079	0.0111
4000 $[km]$	256x64x128	-0.0485	0.0107	-0.0072	-0.0079	0.0110
8000 $[km]$	256x64x256	-0.0485	0.0106	-0.0072	-0.0079	0.0110

where the bottom boundary is the sphere with radius R = 6 371 $[km]$. There, for the simplicity, the Neumann BC in the form $-GM/R^2$, where GM stands for the Geocentric gravitational constant, is taken into account. Then different sized computational domains or different meshing is involved. Results are compared with the exact solution in the form GM/R.

4.2.1 Testing experiment 1

In the first testing experiment, the height of the finite domain Ω_{FE} has been 500 $[km]$, so the finite/infinite element interface has been at height 6 871 $[km]$. Then the center of the infinite elements (which corresponds to the point x_2 in Fig. 6) has been at height 13 742 $[km]$. We have started with the mesh made up of $64 \times 16 \times 4$ nodes, see Table 4, and then we have performed four successive refinements. Results have been compared with the exact solution in the form GM/R.

The statistics of residuals $[m^2 s^{-2}]$ on the bottom boundary Γ computed between the obtained numerical solution and the exact solution can be found in Table 4. One can observe that by refining the mesh, the obtained numerical solution converges to the exact one and that the proposed method is second order accurate, see the EOC column.

4.2.2 Testing experiment 2

For the second testing experiment we have chosen the domain and mesh consisting of $256 \times 64 \times 16$ nodes from *Testing experiment 1*, see Section 4.2.1. Then we have fixed the size of elements while redoubling the radius of the finite element domain. It means that with a doubling of the height of the finite element domain, the number of elements in the vertical direction, see in Table 5, redoubled as well to remain the size of elements. Again, we have compared obtained results with the exact solution in the form GM/R.

The statistics of residuals on the bottom boundary Γ can be seen in Table 5. We can observe that in case of homogeneous sphere, the height of the domain doesn't have impact on the solution on the bottom boundary Γ (Table 6).

4.3 Global gravity field modelling with the EGM2008 data as the reconstruction of the harmonic function

The bottom boundary Γ has been the discretized Earth's surface created with Becker et al. [1] data. The horizontal resolution has been set in accordance with Table 3 presented in Section 4.1, namely 512×128, see Table 7, and 1024×256, see Table 8. The input surface gravity disturbances as BC (2) have been generated from Earth Gravitational Model 2008 (EGM2008) [36]. Then the height of Ω_{FE}, denoted by $H_{\Omega_{FE}}$, has increased gradually from 1000 $[km]$ through 2000, 4000, 5000, 8000 to 16000 $[km]$. Moreover, for each $H_{\Omega_{FE}}$ we have tested five different heights of elements: 200, 100, 50, 25, 12.5 $[km]$ (see Tables 7 and 8). Then the obtained numerical solution on the bottom boundary Γ and at altitude H=200 $[km]$ has been compared to the disturbing potential generated from EGM2008 directly. Statistics of residuals for successive refinements can be found in Tables 7 and 8. In them, we can observe an initial rapid decrease of the stan-

Table 6 *Experiment with gravity data*: Statistics of residuals $[m^2 s^{-2}]$ on the bottom boundary Γ and at H = 200 $[km]$

$H_{\Omega_{FE}}$ = 5000 $[km]$				**0**				H = 200 $[km]$	
No. of nodes	ΔH	Min	Max	Mean	STD	Min	Max	Mean	STD
512x128x57	40	-180.58	174.43	-10.19	14.58	-50.94	26.19	-9.93	7.59
1024x256x112	20	-75.47	76.29	-5.54	4.97	-22.60	2.21	-5.39	2.47
2048x512x222	10	-35.37	23.19	-1.67	1.82	-7.94	1.64	-1.62	1.25
4096x1024x442	5	-36.32	9.39	-0.85	1.16	-4.87	2.18	-0.82	1.03

Table 7 *Experiment with gravity data with the horizontal resolution fixed to:* 512 × 128: Statistics of residuals $[m^2 s^{-2}]$ on the bottom boundary Γ and at H = 200 $[km]$

$H_{\Omega_{FE}} = 1000\,[km]$			**0**				H = 200 $[km]$		
No. of nodes	ΔH	Min	Max	Mean	STD	Min	Max	Mean	STD
512x128x7	200	-114.010	96.589	-11.318	19.412	-82.176	40.908	-10.998	17.823
512x128x12	100	-149.230	139.525	-10.387	20.015	-70.451	39.610	-10.094	17.517
512x128x22	50	-178.549	169.058	-9.751	21.007	-68.898	40.102	-9.478	17.444
512x128x42	25	-191.266	181.196	-9.478	21.553	-68.379	40.362	-9.213	17.420
512x128x82	12.5	-195.152	184.804	-9.394	21.735	-68.230	40.444	-9.132	17.413
$H_{\Omega_{FE}} = 2000\,[km]$			**0**				H = 200 $[km]$		
No. of nodes	ΔH	Min	Max	Mean	STD	Min	Max	Mean	STD
512x128x12	200	-105.005	99.781	-11.716	12.712	-62.381	30.497	-11.401	9.832
512x128x22	100	-146.266	138.745	-10.787	13.770	-54.996	25.310	-10.500	9.454
512x128x42	50	-175.587	167.300	-10.151	15.221	-54.467	28.980	-9.884	9.377
512x128x82	25	-188.304	179.464	-9.879	15.981	-54.259	30.407	-9.620	9.352
512x128x162	12.5	-192.191	183.080	-9.795	16.230	-54.194	30.809	-9.539	9.345
$H_{\Omega_{FE}} = 4000\,[km]$			**0**				H = 200 $[km]$		
No. of nodes	ΔH	Min	Max	Mean	STD	Min	Max	Mean	STD
512x128x22	200	-104.412	104.273	-11.865	11.473	-58.356	29.203	-11.552	8.126
512x128x42	100	-145.673	143.271	-10.938	12.699	-52.199	23.443	-10.652	7.755
512x128x82	50	-174.995	169.470	-10.302	14.272	-51.760	25.690	-10.036	7.681
512x128x162	25	-187.715	180.041	-10.029	15.083	-51.553	26.413	-9.772	7.655
512x128x322	12.5	-191.602	183.153	-9.945	15.348	-51.488	26.620	-9.691	7.648
$H_{\Omega_{FE}} = 5\,000\,[km]$			**0**				H = 200 $[km]$		
No. of nodes	ΔH	Min	Max	Mean	STD	Min	Max	Mean	STD
512x128x27	200	-104.433	104.667	-11.879	11.424	-57.691	29.619	-11.567	8.054
512x128x52	100	-145.693	143.668	-10.951	12.660	-51.443	23.859	-10.666	7.687
512x128x102	50	-175.017	169.868	-10.316	14.238	-51.023	26.106	-10.050	7.612
512x128x202	25	-187.736	180.440	-10.043	15.050	-50.817	26.829	-9.786	7.586
512x128x402	12.5	-191.623	183.553	-9.959	15.316	-50.752	27.037	-9.705	7.579
$H_{\Omega_{FE}} = 6\,000\,[km]$			**0**				H = 200 $[km]$		
No. of nodes	ΔH	Min	Max	Mean	STD	Min	Max	Mean	STD
512x128x32	200	-104.450	104.827	-11.884	11.408	-57.330	29.788	-11.572	8.031
512x128x62	100	-145.711	143.828	-10.957	12.648	-50.996	24.027	-10.672	7.666
512x128x122	50	-175.035	170.029	-10.322	14.227	-50.586	26.275	-10.056	7.591
512x128x242	25	-187.754	180.601	-10.049	15.040	-50.379	26.999	-9.792	7.564
512x128x482	12.5	-191.641	183.714	-9.965	15.306	-50.314	27.206	-9.711	7.557
$H_{\Omega_{FE}} = 8\,000\,[km]$			**0**				H = 200 $[km]$		
No. of nodes	ΔH	Min	Max	Mean	STD	Min	Max	Mean	STD
512x128x42	200	-104.460	104.925	-11.889	11.400	-57.004	29.891	-11.576	8.018
512x128x82	100	-145.721	143.928	-10.961	12.642	-50.561	24.132	-10.676	7.654
512x128x162	50	-175.045	170.129	-10.326	14.221	-50.162	26.381	-10.060	7.578
512x128x322	25	-187.765	180.701	-10.053	15.034	-49.955	27.104	-9.796	7.551
512x128x642	12.5	-191.652	183.814	-9.969	15.299	-49.890	27.312	-9.714	7.543
$H_{\Omega_{FE}} = 16\,000\,[km]$			**0**				H = 200 $[km]$		
No. of nodes	ΔH	Min	Max	Mean	STD	Min	Max	Mean	STD
512x128x82	200	-104.445	104.947	-11.890	11.395	-56.787	29.912	-11.577	8.011
512x128x162	100	-145.706	143.950	-10.962	12.637	-50.254	24.156	-10.677	7.647
512x128x322	50	-175.031	170.152	-10.327	14.216	-49.861	26.405	-10.061	7.569
512x128x642	25	-187.750	180.723	-10.054	15.029	-49.655	27.129	-9.797	7.542
512x128x1282	12.5	-191.637	183.837	-9.970	15.295	-49.589	27.336	-9.716	7.534

Table 8 *Experiment with gravity data with the horizontal resolution fixed to:* 1024×256: Statistics of residuals $[m^2 s^{-2}]$ on the bottom boundary Γ and at H = 200 $[km]$

$H_{\Omega_{FE}} = 1000\,[km]$			**0**				H = 200 $[km]$		
No. of nodes	ΔH	Min	Max	Mean	STD	Min	Max	Mean	STD
1024x256x7	200	-94.444	55.892	-8.033	16.760	-60.892	42.143	-7.783	16.349
1024x256x12	100	-67.653	42.543	-6.887	16.152	-50.765	41.010	-6.669	16.038
1024x256x22	50	-70.701	65.150	-5.808	16.117	-48.038	42.105	-5.621	15.934
1024x256x42	25	-70.669	65.146	-5.809	16.109	-48.006	42.072	-5.622	15.926
1024x256x82	12.5	-75.076	83.793	-4.821	16.296	-46.328	43.222	-4.663	15.875
$H_{\Omega_{FE}} = 2000\,[km]$			**0**				H = 200 $[km]$		
No. of nodes	ΔH	Min	Max	Mean	STD	Min	Max	Mean	STD
1024x256x12	200	-89.120	43.966	-8.389	7.688	-41.025	13.784	-8.146	6.462
1024x256x22	100	-60.473	22.189	-7.283	6.734	-27.434	7.735	-7.070	6.041
1024x256x42	50	-63.443	53.274	-6.205	6.735	-25.287	8.476	-6.024	5.835
1024x256x82	25	-68.544	74.323	-5.507	7.026	-24.206	9.211	-5.347	5.742
1024x256x162	12.5	-70.771	81.381	-5.218	7.198	-23.778	9.527	-5.066	5.710
$H_{\Omega_{FE}} = 4000\,[km]$			**0**				H = 200 $[km]$		
No. of nodes	ΔH	Min	Max	Mean	STD	Min	Max	Mean	STD
1024x256x22	200	-91.212	46.271	-8.576	5.880	-40.105	13.547	-8.333	3.974
1024x256x42	100	-65.149	21.924	-7.432	4.459	-28.441	2.256	-7.221	3.182
1024x256x82	50	-68.597	52.273	-6.355	4.471	-24.494	1.741	-6.175	2.779
1024x256x162	25	-73.682	73.322	-5.656	4.890	-22.240	1.843	-5.497	2.558
1024x256x322	12.5	-75.903	80.380	-5.367	5.130	-21.349	1.946	-5.217	2.476
$H_{\Omega_{FE}} = 5000\,[km]$			**0**				H = 200 $[km]$		
No. of nodes	ΔH	Min	Max	Mean	STD	Min	Max	Mean	STD
1024x256x27	200	-91.502	46.555	-8.589	5.867	-41.290	13.838	-8.346	3.943
1024x256x52	100	-65.912	22.493	-7.446	4.452	-29.225	2.535	-7.235	3.156
1024x256x102	50	-69.411	52.015	-6.368	4.459	-25.276	2.032	-6.189	2.740
1024x256x202	25	-74.494	73.063	-5.670	4.873	-23.021	2.141	-5.511	2.507
1024x256x402	12.5	-76.714	80.121	-5.381	5.112	-22.129	2.244	-5.231	2.418
$H_{\Omega_{FE}} = 6000\,[km]$			**0**				H = 200 $[km]$		
No. of nodes	ΔH	Min	Max	Mean	STD	Min	Max	Mean	STD
1024x256x32	200	-91.680	46.717	-8.595	5.889	-41.912	14.004	-8.352	3.970
1024x256x62	100	-66.509	22.782	-7.452	4.486	-29.640	2.702	-7.241	3.194
1024x256x122	50	-69.837	51.885	-6.374	4.488	-25.689	2.199	-6.195	2.777
1024x256x242	25	-74.920	72.933	-5.676	4.896	-23.433	2.312	-5.517	2.541
1024x256x482	12.5	-77.139	79.990	-5.387	5.132	-22.541	2.415	-5.237	2.450
$H_{\Omega_{FE}} = 8000\,[km]$			**0**				H = 200 $[km]$		
No. of nodes	ΔH	Min	Max	Mean	STD	Min	Max	Mean	STD
1024x256x42	200	-91.858	46.874	-8.598	5.928	-42.458	14.163	-8.355	4.020
1024x256x82	100	-67.058	23.043	-7.455	4.537	-30.005	2.863	-7.245	3.258
1024x256x162	50	-70.211	51.785	-6.378	4.534	-26.054	2.358	-6.199	2.842
1024x256x322	25	-75.293	72.834	-5.680	4.935	-23.797	2.475	-5.521	2.605
1024x256x642	12.5	-77.512	79.891	-5.391	5.167	-22.905	2.578	-5.240	2.514
$H_{\Omega_{FE}} = 16000\,[km]$			**0**				H = 200 $[km]$		
No. of nodes	ΔH	Min	Max	Mean	STD	Min	Max	Mean	STD
1024x256x82	200	-91.992	46.985	-8.600	5.965	-42.803	14.275	-8.357	4.070
1024x256x162	100	-67.405	23.229	-7.457	4.584	-30.238	2.977	-7.246	3.317
1024x256x322	50	-70.448	51.749	-6.379	4.577	-26.286	2.471	-6.200	2.903
1024x256x642	25	-75.529	72.798	-5.681	4.970	-24.029	2.590	-5.522	2.666
1024x256x1282	12.5	-77.748	79.854	-5.392	5.200	-23.137	2.693	-5.242	2.574

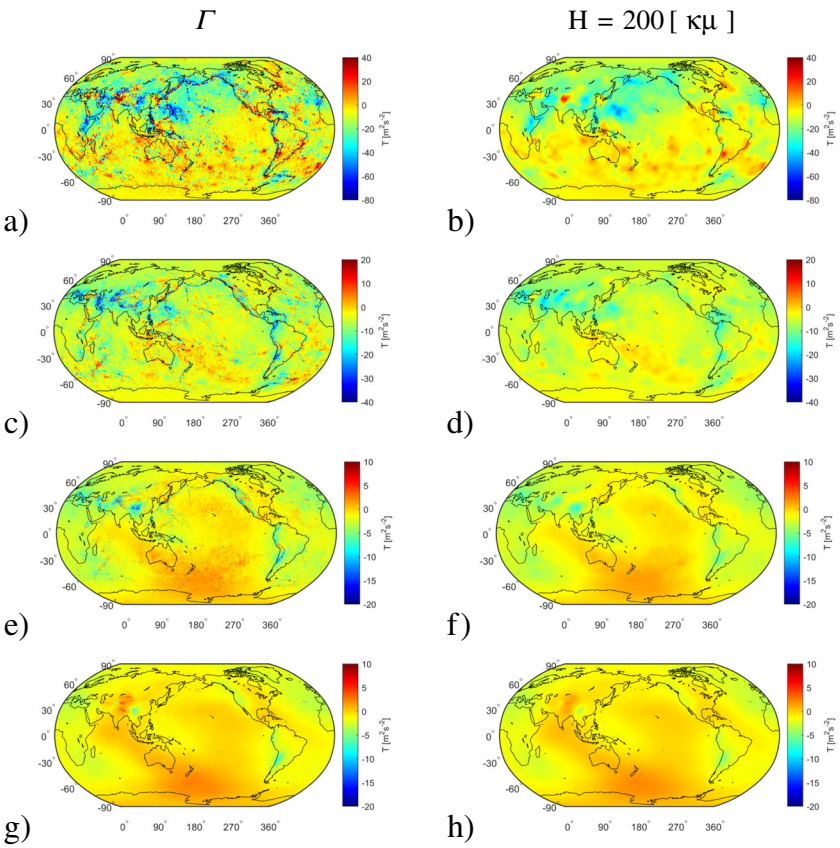

Fig. 11 Residuals between the FEM solutions and the disturbing potential obtained from EGM2008 directly. In the left column, one can see residuals at Γ, in the right column at height 200 $[km]$. Resolutions are: a), b) 512x128x57, c), d) 1024x256x112, e), f) 2048x512x222, g), h) 4096x1024x442

dard deviation of residuals with an increase of $H_{\Omega_{FE}}$, see the STD columns, which stagnates at approximately $H_{\Omega_{FE}}$ = 5000 $[km]$. Also in case of $H_{\Omega_{FE}}$ = 1000 $[km]$, we can see that the standard deviations of residuals are very similar for both horizontal resolutions, however, with an increase of $H_{\Omega_{FE}}$ the difference between them is growing and stagnates at appropriately $H_{\Omega_{FE}}$ = 5000 $[km]$. We can also observe an improvement of mean value of residuals when refining the mesh in the vertical direction. Also, it is not surprising that the standard deviation of residuals is better at H=200 $[km]$ than at Γ, since the disturbing potential solution smooths with increasing heights. When we look closely at the Table 7, we can observe that if we are interested only in a solution on Γ, it is better to have fewer elements in the vertical direction. On the other hand, for the solution at H = 200 $[km]$ it is better to have more elements in the vertical direction (see Min, Max and STD columns). According to our opinion, this strange behaviour is caused by a very coarse grid in the horizontal direction, what is then confirmed by Table 8.

Based on the these results, we have decided to execute a more detailed experiment using only $H_{\Omega_{FE}}$ = 5000 $[km]$. To study the convergence of the numerical solution, we have chosen successive resolutions with the number of all nodes 512 × 128 × 57, 1024 × 256 × 112, 2048 × 512 × 222 and the most detailed one 4096 × 1024 × 442, where the finest resolution corresponds to our maximum computing capabilities. In the vertical direction, we have decided to have a more detailed solution in to 200 $[km]$ (the height of elements ΔH is presented in the second column of Table 6) and then we have doubled it. The obtained residuals are visualised in Fig. 11 and their corresponding statistics is presented in Table 6. We can observe an improvement of all statistical characteristics when refining the computational grid, which proves the validity of the presented FEM approach to the global gravity field modelling.

5 Conclusion and summary

In the presented paper, a novel numerical approach for solving the original FGBVP including the condition of the regularity at infinity was developed. Here, the numerical scheme based on the FEM with finite and mapped infinite elements was derived and implemented. In numerical experiments, at first, a convergence of the proposed numerical scheme to the exact solution in different situations was studied. It was shown that in the case of potential generated by a homogeneous sphere, the proposed numerical approach is second order accurate. Then a numerical study focused on a reconstruction of the harmonic function (EGM2008) above the discretized Earth's topography was done. The obtained

numerical solutions were tested at nodes on the Earth's surface as well as nodes lying approximately at the altitude of the GOCE satellite mission. Gained results showed a practical contribution of the presented approach to global gravity field modelling.

Acknowledgements This work was supported by Grants APVV-19-0460, VEGA 1/0486/20 and VEGA 1/0436/20.

Author Contributions Marek Macák developed the theory and performed the numerical simulations. Zuzana Minarechová contributed to develop the theory and wrote the manuscript. Lukáš Tomek developed the meshing of the computational domain. Róbert Čunderlík and Karol Mikula devised the project. All authors discussed the results and contributed to the final manuscript.

Funding Open access funding provided by The Ministry of Education, Science, Research and Sport of the Slovak Republic in cooperation with Centre for Scientific and Technical Information of the Slovak Republic

Data Availibility Statement All datasets generated and/or analysed within the experiments are available from the corresponding author.

Declarations

Conflict of Interests/Competing Interests All authors declare that they have no conflicts of interest.

References

1. Becker, J.J., Sandwell, D.T., Smith, W.H.F., Braud, J., Binder, B., Depner, J., Fabre, D., Factor, J., Ingalls, S., Kim, S.H., Ladner, R., Marks, K., Nelson, S., Pharaoh, A., Trimmer, R., Von Rosenberg, J., Wallace, G., Weatherall, P.: Global Bathymetry and Elevation Data at 30 Arc Seconds Resolution: SRTM30 PLUS. Marine Geodesy **32**(4), 355–371 (2009)
2. Bettess, P.: Infinite elements. International Journal for Numerical Methods in Engineering **11**(1), 53–64 (1977)
3. Bettess, P.: More on infinite elements. International Journal for Numerical Methods in Engineering **15**(11), 1613–1626 (1983)
4. Bjerhammar, A., Svensson, L.: On the geodetic boundary value problem for a fixed boundary surface. A satellite approach. Bulletin Géodésique **57**(1–4), 382–393 (1983)
5. Brenner, S.C., Scott, L.R.: The mathematical theory of finite element methods. Springer-Verlag, New York (2002)
6. B. Bucha, J. Janák, A MATLAB-based graphical user interface program for computing functionals of the geopotential up to ultra-high degrees and orders. Computers & Geosciences 56, 186-196 http://dx.doi.org/10.1016/j.cageo.2013.03.012 (2013)
7. Čunderlík, R., Mikula, K., Mojžeš, M.: Numerical solution of the linearized fixed gravimetric boundary-value problem. Journal of Geodesy **82**, 15–29 (2008)
8. Čunderlík, R., Mikula, K.: Direct BEM for high-resolution gravity field modelling. Studia Geophysica et Geodaetica **54**(2), 219–238 (2010)
9. Čunderlík, R., Mikula, K., Špir, R.: An oblique derivative in the direct BEM formulation of the fixed gravimetric BVP. International Association of Geodesy Symposia **137**, 227–231 (2012)
10. Damjanic, F., Owen, D.R.J.: Mapped infinite element in transient thermal analysis. Computers & Structures **19**, 673–687 (1984)
11. Droniou, J., Medl'a, M., Mikula, K.: Design and analysis of finite volume methods for elliptic equations with oblique derivatives; application to Earth gravity field modeling. Journal of Computational Physics **398**, 108876 (2019). https://doi.org/10.1016/j.jcp.2019.108876
12. Fašková, Z., Čunderlík, R., Janák, J., Mikula, K., Šprlák, M.: Gravimetric quasigeoid in Slovakia by the finite element method. Kybernetika **43**(6), 789–796 (2007)
13. Z. Fašková, Numerical Methods for Solving Geodetic Boundary Value Problems. PhD Thesis, SvF STU, Bratislava, Slovakia, (2008)
14. Fašková, Z., Čunderlík, R., Mikula, K.: Finite element method for solving geodetic boundary value problems. Journal of Geodesy **84**(2), 135–144 (2010)
15. Freeden, W., Kersten, H.: A constructive approximation theorem for the oblique derivative problem in potential theory. Mathematical Methods in Applied Sciences **3**, 104–114 (1981)
16. Holota, P.: Coerciveness of the linear gravimetric boundary-value problem and a geometrical interpretation. Journal of Geodesy **71**, 640–651 (1997)
17. Kaiming, X., Zhijun, Z.: Three-dimensional finite/infinite elements analysis of fluid flow in porous media. Applied Mathematical Modelling **30**(9), 904–919 (2006)
18. W. Keller, Finite differences schemes for elliptic boundary value problems. Section IV Bulletin IAG, No. 1. (1995)
19. Klees, R.: Boundary value problems and approximation of integral equations by finite elements. Manuscripta Geodaetica **20**, 345–361 (1995)
20. Koch, K.R., Pope, A.J.: Uniqueness and existence for the geodetic boundary value problem using the known surface of the earth. Bulletin Géodésique **46**, 467–476 (1972)
21. Kumar, P.: Infinite elements for numerical analysis of underground excavations. Tunnelling and Underground Space Technology **15**(1), 117–124 (2000)
22. Lehmann, R., Klees, R.: Numerical solution of geodetic boundary value problems using a global reference field. Journal of Geodesy **73**, 543–554 (1999)
23. G.M. Lieberman, Oblique Derivative Problems for Elliptic Equations, World Scientific Publishing Co. Pte. Ltd., Hackensack, NJ, ISBN: 978-981-4452-32-8 (2013)
24. M. Macák, R. Čunderlík, K. Mikula, Z. Minarechová, An upwind-based scheme for solving the oblique derivative boundary-value problem related to the physical geodesy. Journal of Geodetic Science, Volume 5, Issue 1, (2015)
25. Macák, M., Čunderlík, R., Mikula, K., Minarechová, Z.: Computational optimization in solving the geodetic boundary value

problems. Discrete & Continuous Dynamical Systems - S **14**(3), 987–999 (2021)
26. M. Macák, K. Mikula, Z. Minarechová, Solving the oblique derivative boundary-value problem by the finite volume method, ALGORITMY 2012, 19th Conference on Scientific Computing, Podbanske, Slovakia, September 9-14, 2012, Proceedings of contributed papers and posters, Publishing House of STU, 75-84 (2012)
27. M. Macák, Z. Minarechová K. Mikula, A novel scheme for solving the oblique derivative boundary-value problem, Studia Geophysica et Geodaetica 58(4): 556-570, (2014)
28. Macák, M., Minarechová, Z., Čunderlík, R., Mikula, K.: The finite element method as a tool to solve the oblique derivative boundary value problem in geodesy. Tatra Mountains Mathematical Publications. **75**(1), 63–80 (2020)
29. Marques, J.M.M.C., Owen, D.R.J.: Infinite elements in quasi-static materially nonlinear problems. Computers & Structures **18**(4), 739–751 (1984)
30. MATLAB version 2018 b, Natick, Massachusetts: The MathWorks Inc., 2018
31. Medl'a, M., Mikula, K., Čunderlík, R., Macák, M.: Numerical solution to the oblique derivative boundary value problem on non-uniform grids above the Earth topography. Journal of Geodesy **92**, 1–19 (2018)
32. P. Meissl, The use of finite elements in physical geodesy. Report 313, Geodetic Science and Surveying, The Ohio State University, (1981)
33. Minarechová, Z., Macák, M., Čunderlík, R., Mikula, K.: High-resolution global gravity field modelling by the finite volume method. Studia Geophysica et Geodaetica **59**, 1–20 (2015)
34. Minarechová, Z., Macák, M., Čunderlík, R., Mikula, K.: On the finite element method for solving the oblique derivative boundary value problems and its application in local gravity field modelling. Journal of Geodesy **95**, 70 (2021)
35. D. Mráz, M. Bořík, J. Novotný, On the Convergence of the h-p Finite Element Method for Solving Boundary Value Problems in Physical Geodesy, Freymueller J.T., Sánchez L. (eds) International Symposium on Earth and Environmental Sciences for Future Generations. International Association of Geodesy Symposia, vol 147. Springer, Cham (2016)
36. Pavlis, N.K., Holmes, S.A., Kenyon, S.C., Factor, J.K.: The development and evaluation of the Earth Gravitational Model 2008 (EGM2008). Journal of Geophysical Research **117**, B04406 (2012). https://doi.org/10.1029/2011JB008916
37. J.N. Reddy, An Introduction to the Finite Element Method, 3rd Edition, McGraw-Hill Education, New York, ISBN: 9780072466850 (2006)
38. Shaofeng, B., Dingbo, C.: The finite element method for the geodetic boundary value problem. Manuscripta geodaetica **16**, 353–359 (1991)
39. Simoni, L., Schrefler, B.A.: Mapped infinite elements in soil consolidation. International Journal for Numerical Methods in Engineering **24**, 513–527 (1987)
40. G.L.G. Sleijpen, D.R. Fokkema, Bicgstab (l) for Linear Equations Involving Unsymmetric Matrices with Complex Spectrum, http://dspace.library.uu.nl/handle/1874/16827, (1993)
41. Šprlák, M., Fašková, Z., Mikula, K.: On the application of the coupled finite-infinite element method to the geodetic boundary value problem. Studia Geophysica et Geodaetica **55**, 479–487 (2011)
42. Xia, K., Bai, M.: Modeling fluid flow and solid deformation in naturally fractured reservoirs. The University of Oklahoma, Norman, Rock Mechanics Institute (1998)
43. Yin, Z., Sneeuw, N.: Modeling the gravitational field by using CFD techniques. Journal of Geodesy **95**, 68 (2021). https://doi.org/10.1007/s00190-021-01504-w
44. Zienkiewicz, O.C., Emson, C., Bettess, P.: A novel boundary infinite element. International Journal for Numerical Methods in Engineering **19**, 340–393 (1983)
45. Zienkiewicz, O.C., Bando, K., Bettess, P., Emson, C., Chiam, T.C.: Mapped infinite elements for exterior wave problems. International Journal for Numerical Methods in Engineering **21**, 1229–1251 (1985)